

Structure of the European upper mantle revealed by adjoint tomography

Hejun Zhu^{1*}, Ebru Bozdağ¹, Daniel Peter¹ and Jeroen Tromp^{1,2}

Images of the European crust and upper mantle, created using seismic tomography, identify the Cenozoic Rift System and related volcanism in central and western Europe. They also reveal subduction and slab roll back in the Mediterranean-Carpathian region^{1–12}. However, existing tomographic models are either high in resolution, but cover only a limited area^{13,14}, or low in resolution, and thus miss the finer-scale details of mantle structure^{5,12}. Here we simultaneously fit frequency-dependent phase anomalies of body and surface waveforms in complete three-component seismograms with an iterative inversion strategy involving adjoint methods, to create a tomographic model of the European upper mantle. We find that many of the smaller-scale structures such as slabs, upwellings and delaminations that emerge naturally in our model are consistent with existing images. However, we also derive some hitherto unidentified structures. Specifically, we interpret fast seismic-wave speeds beneath the Dinarides Mountains, southern Europe, as a signature of northeastward subduction of the Adria plate; slow seismic-wave speeds beneath the northern part of the Rhine Graben as a reservoir connected to the Eifel hotspot; and fast wave-speed anomalies beneath Scandinavia as a lithospheric drip, where the lithosphere is delaminating and breaking away. Our model sheds new light on the enigmatic palaeotectonic history of Europe.

To make seismic tomography computationally feasible, traditional studies generally adopt a one-dimensional reference model and approximate, asymptotic methods for the calculation of travel times or synthetic seismograms. Modern numerical methods, such as the spectral element method¹⁵, in combination with fast, parallel computers have facilitated iterative, nonlinear tomographic inversions based on more realistic three-dimensional (3D) initial models and fully numerical simulations. These numerical methods may be exploited within the minimization problem by using adjoint techniques^{16–19}, a procedure we refer to as adjoint tomography^{20–22}. The main advantages of this approach are the calculation of accurate seismograms and Fréchet derivatives in complex 3D models, avoidance of widely used crustal corrections by jointly inverting for structure in the mantle and crust, and exploitation of complete broadband three-component seismograms by simultaneously fitting body and surface waves.

Existing tomographic models of the European mantle may be roughly subdivided into two broad categories: body-wave models based on inversion of compressional or shear-wave travel-time anomalies^{2–4,7,10,11,13,14} and surface-wave models based on inversion of Love- and Rayleigh-wave dispersion measurements or waveform differences^{5,12}. The goal here is to bridge the gap between these two types of inversion by simultaneously fitting frequency-dependent

phase anomalies of numerous body and surface waveforms in complete three-component seismograms, thereby effectively using entire seismographic records.

Our 3D starting model, EU₀₀, consists of crustal model EPcrust²³ in combination with transversely isotropic mantle model S362ANI (ref. 24); the latter employs 1D background model STW105 (ref. 24). Iterative transversely isotropic model updates are parameterized in terms of bulk sound-wave speed c , vertically and horizontally polarized shear-wave speeds β_v and β_h and the dimensionless parameter η ; density perturbations are scaled to isotropic shear-wave-speed perturbations (see Supplementary Information S4). This transversely isotropic parameterization is important for resolving the Rayleigh/Love discrepancy²⁵. In the interest of space, we focus our discussion on the vertically polarized shear-wave speed β_v .

We use data from 190 earthquakes recorded by 745 seismographic stations (Supplementary Fig. S2), resulting in 26,581 useable three-component seismograms. Before the structural inversion, we reinvert centroid-moment tensor solutions for all events in the database; the source mechanisms remain largely unchanged, but we see a previously noted systematic shallowing of suboceanic hypocentres²⁶ (see Supplementary Fig. S5).

Frequency-dependent travel-time differences between simulated and recorded three-component seismic waveforms—normalized by their standard deviations—are used to characterize misfit in the inversion²⁷. The nondimensional total misfit function consists of two contributions: body waves with periods between 15 s and 50 s and surface waves with initial periods between 50 s and 150 s; as the inversion progresses, the short-period surface-wave corner is gradually reduced from 50 s to 25 s and the long-period corner is decreased from 150 s to 100 s, thereby steadily resolving smaller-scale structures. For both contributions, we monitor the behaviour of the misfit on all three components; the total misfit function is the sum of these six contributions. As illustrated in Fig. 1, with each iteration the misfit is reduced for all six contributions and the total misfit diminishes from 5.05 to 2.45. As the model improves, the number of measurement windows increases, thereby gradually providing more-detailed structural information. After 18 iterations, we included 31 new earthquakes and additional data—primarily from arrays and networks in Iceland and Turkey—to further constrain the model. The additional data led to a step increase in the number of measurements, which continues to grow in subsequent iterations, culminating in 123,205 measurement windows. The extra data come at the cost of a temporary increase in misfit values, which is gradually reduced over the subsequent 12 iterations (see Supplementary Information S1). The overall misfit shown in Fig. 1a levels off at iteration 30 on a slightly elevated level compared with

¹Department of Geosciences, Princeton University, Princeton, New Jersey, 08544, USA, ²Program in Applied and Computational Mathematics, Princeton University, Princeton, New Jersey, 08544, USA. *e-mail: hejunzhu@princeton.edu.

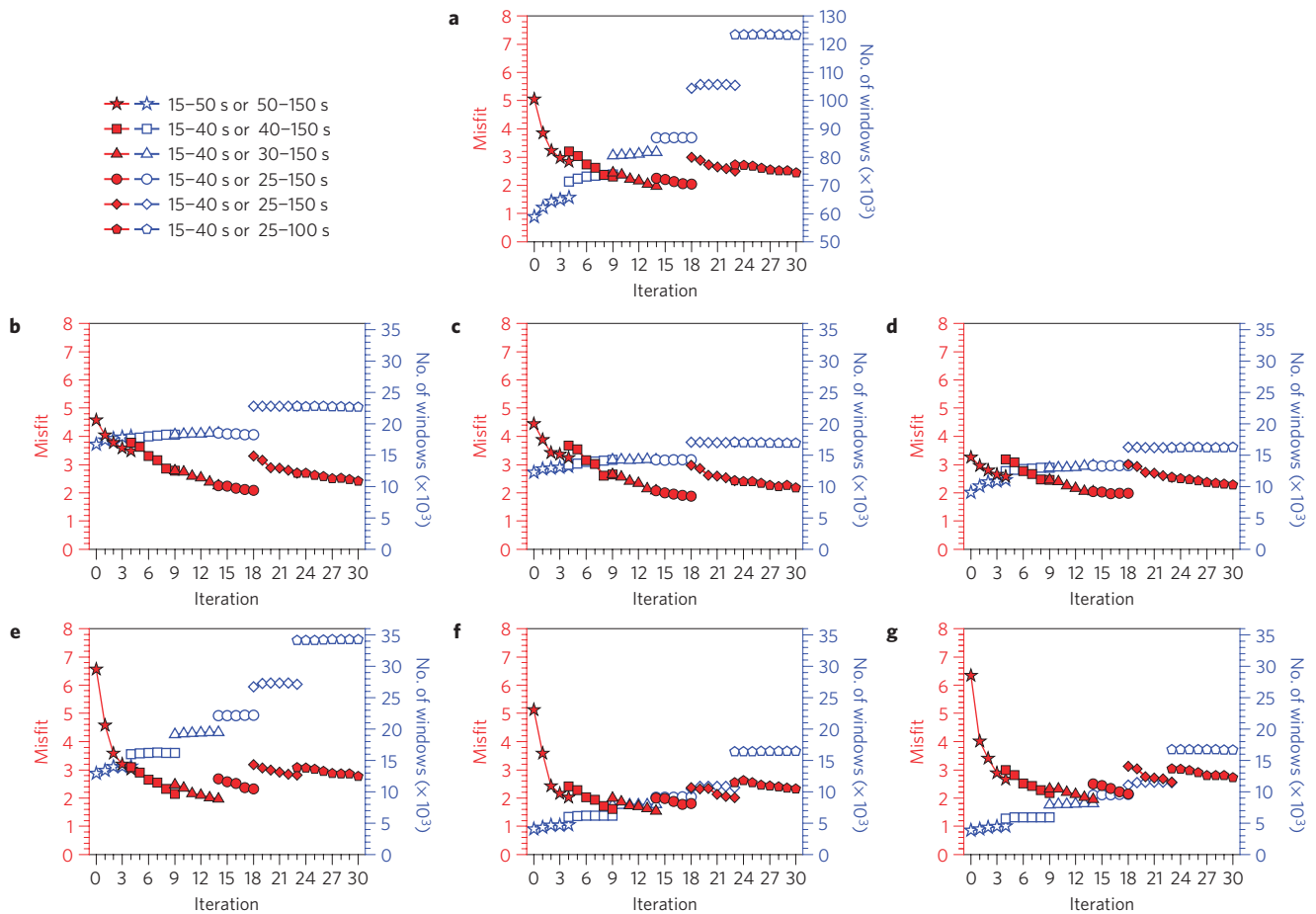


Figure 1 | Behaviour of the misfit function and the number of measurement windows as a function of iteration. Filled red symbols denote misfit values and open blue symbols denote the number of measurements. **a**, Evolution of the total misfit function. **b–d**, Three-component, short-period body-wave contributions on the vertical and radial (P–SV) and transverse (SH) components, respectively. **e–g**, Three-component, long-period surface-wave contributions on the vertical and radial (Rayleigh) and transverse (Love) components, respectively. For body waves, we use a 15–50 s band pass for the first four iterations, followed by a 15–40 s band pass in subsequent iterations. For surface waves, the long period corner is 150 s for the first 23 iterations, followed by 100 s in subsequent iterations. The short-period corner is gradually decreased from 50 s to 25 s. After 18 iterations, 31 additional earthquakes and data from several IRIS/PASSCAL deployments and the Kandilli Observatory were added to the data set, resulting in an increase in the number of measurement windows at the cost of a transient increase in misfit.

its value at iteration 18 owing to the relatively poorer quality of the additional array data as compared with data from permanent arrays. After 30 iterations, we obtain a new European crustal and upper-mantle model named EU₃₀, which requires a total of 17,100 wavefield simulations and 2.3 million central processing unit hours. Compared with the starting model, both the mean values and standard deviations for all six contributions in Fig. 1 are significantly reduced (see Supplementary Fig. S6).

We present map views (Fig. 2) and vertical cross-sections (Fig. 3) of relative perturbations in β_v for model EU₃₀ with respect to 1D background model STW105 (ref. 24). Map views and cross-sections of EU₀₀ and intermediate model EU₁₈ are provided in Supplementary Figs S8–S11. At 75 km depth (Fig. 2a), one of the most striking features is the Tornquist–Teisseyre Zone (TTZ) separating the Precambrian East European Platform (EEP) from Phanerozoic central and eastern Europe⁵. The TTZ has become much sharper in the final model, EU₃₀, when compared with the starting model, EU₀₀. Model EU₃₀ reveals a variety of localized fast wave-speed anomalies (Fig. 2a), including the Central Graben in the North Sea, the Armorican Massif in northwestern France and a tilted Y-shaped anomaly related to a triple junction of Mediterranean plate boundaries. We also observe a lithospheric drip associated with delamination beneath Scandinavia (Fig. 3d),

consistent with an image determined in a previous study²⁸. In map view at 75 km depth (Fig. 2a), we note a striking absence of fast shear-wave speeds below western Norway, which may explain the existence of its coastal mountain ranges.

In our interpretations we focus on three arc systems, namely, the Apennines–Calabrian–Maghrebides, Carpathian–Vrancea–Adria, and Hellenic–Cyprus arcs, as well as two large low-wave-speed systems, namely, the Cenozoic Rift System in central and western Europe and the Anatolian plate. The Apennines–Calabrian–Maghrebides arc started to roll back 30 million years ago, generating slab detachments during the retreat to its present location⁸. Slab detachments in the form of discontinuous fast anomalies are observed beneath the central Apennines in Italy and the Maghrebides in North Africa (Fig. 3g). Beneath the Calabrian arc segment we find a clear gap between shallow lithosphere and deep fast anomalies, indicating that a speculated slab detachment⁸ also exists for this portion of the arc system (Fig. 3f). There is a large volume of fast material lying on top of the lower mantle, at 625 km depth, beneath the western Mediterranean Sea (Fig. 2e), which is attributed to the roll back of this arc system. The Tyrrhenian Sea and Algero–Provençal Basin are revealed as slow anomalies down to 200 km and were produced as a result of back-arc extension associated with the roll back. Beneath the Alpine belt,

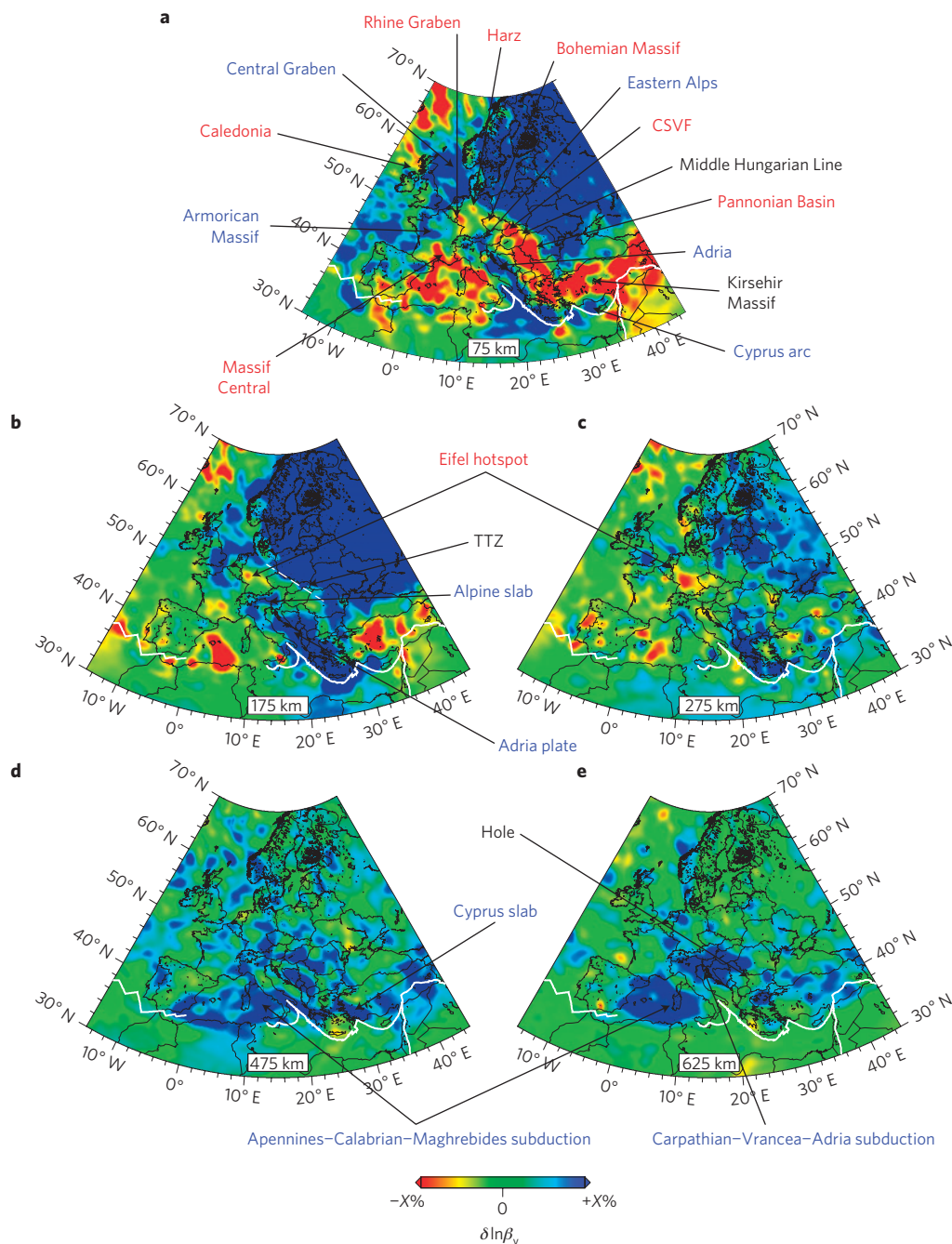


Figure 2 | Horizontal cross-sections of relative perturbations in β_v , $\delta \ln \beta_v$, for model EU₃₀. a, 75 km, b, 175 km, c, 275 km, d, 475 km and e, 625 km. Colours show relative wave-speed perturbations with respect to 1D background model STW105 (ref. 24). Perturbations range from $-X\%$ to $+X\%$, where $X = 4$ in **a and $X = 3$ in **b–e**. Major tectonic features are labelled (see Supplementary Fig. S1). x-axis labels denote longitude, y-axis labels denote latitude. CSVF, Central Slovakian Volcanic Field; TTZ, Tornquist–Teisseyre Zone.**

a fast anomaly is imaged down to nearly 400 km, which overlays the Apennines–Calabrian–Maghrebides slab (Fig. 3c). At 175 km depth, the Alpine slab shows a striking arcuate shape beneath northern Italy (Fig. 2b).

The slab beneath the western Carpathian part of the Carpathian–Vrancea arc is completely detached from the surface. However, in the eastern Vrancea portion we find a fast anomaly connected with shallow lithosphere and subducted southwestward, in agreement with previous interpretations⁸. In this region we discover another slab associated with northeastward subduction of the Adria plate underneath the Dinarides. At approximately 400 km depth, the Vrancea and Adria–Dinarides slabs meet each other (Figs 3a and 4).

The Vrancea slab continues down to 660 km depth where it piles up as another large volume of fast material beneath eastern Europe (Fig. 2e). Beneath the southern margin of the EEP and adjacent to the Black Sea, we observe lithospheric thickening of the EEP to depths of 400 km (Figs 3a and 4). The Pannonian Basin and forearc are imaged as very large slow anomalies ($\sim -4\%$) down to 120 km depth, lying right above the Vrancea and Adria–Dinarides slabs.

Contrary to the previous two arc systems, which are mainly confined to the upper mantle, the Hellenic slab penetrates through the 660 km discontinuity into the lower mantle (Fig. 3b). Within the transition zone, the Hellenic slab interacts with the Adria–Dinarides and Vrancea slabs, generating a hole beneath Bulgaria²⁹,

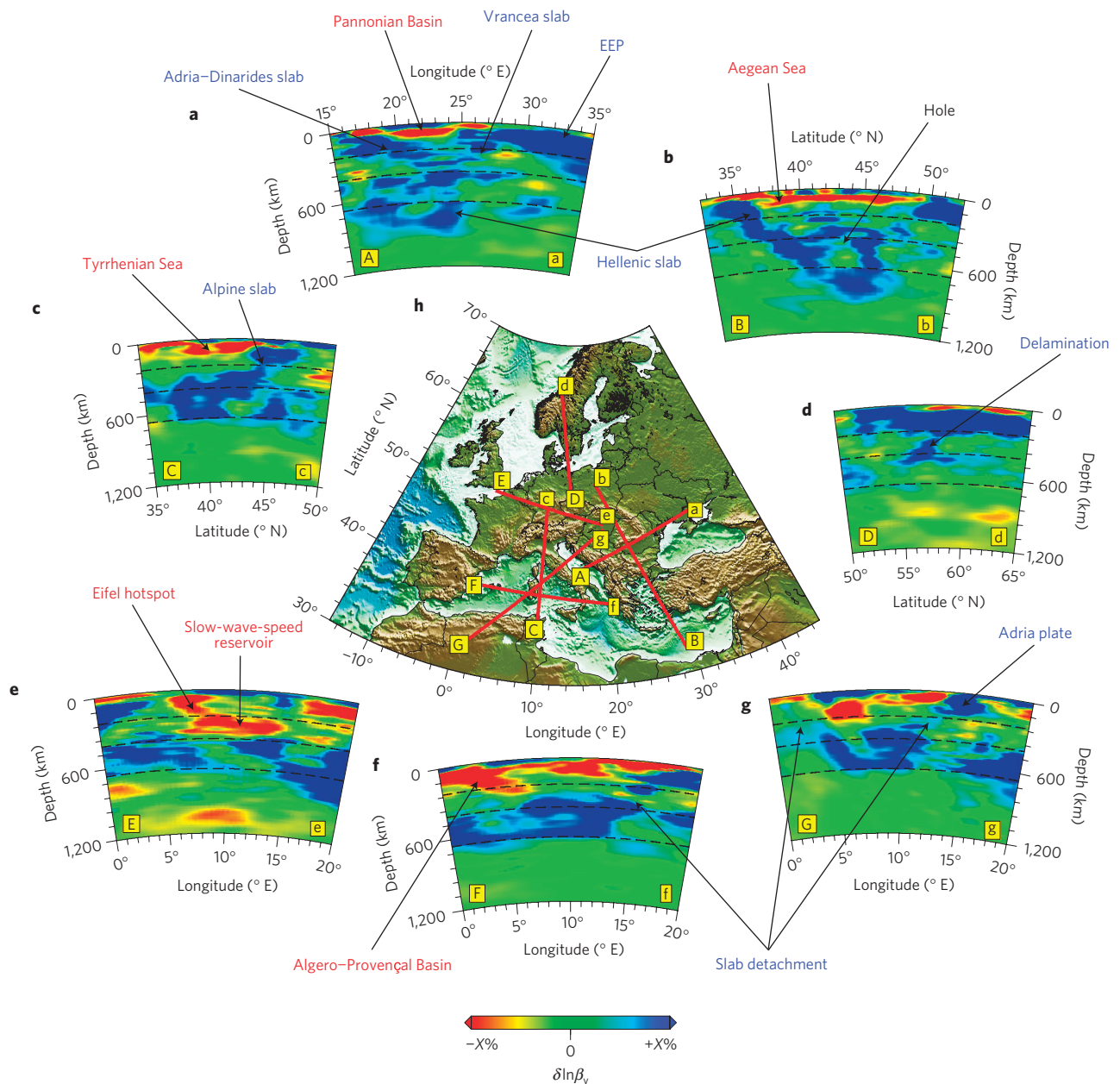


Figure 3 | Vertical cross-sections of $\delta \ln \beta_v$ for model EU₃₀. **a**, Cross-section of the Adria-Dinarides and Vrancea slabs. **b**, Cross-section of the Hellenic slab and a hole beneath Bulgaria. **c**, Cross-section of the Alpine subduction. **d**, Cross-section of lithospheric delamination beneath Scandinavia. **e**, Cross-section of the Eifel hotspot and its associated slow-wave-speed reservoir. **f**, Cross-section of the Calabrian slab detachment. **g**, Cross-section of the central Apennines and North Africa slab detachment. The dashed black lines in **a–g** denote the 220 km, 410 km and 660 km discontinuities. Perturbations range from $-X\%$ to $+X\%$; $X=3$ in all cross-sections except **e**, where $X=2$. **h**, Map locations of cross-sections **a–g** (A–a to G–g).

as documented in map views (Fig. 2e), vertical cross-sections (Fig. 3b) and 3D view (Fig. 4). At 75 km depth, there is a fast spot located east of the Hellenic arc, between the Cyprus and Anatolian plates, which is correlated with the Cyprus arc (Fig. 2a). Similar to the two previously discussed arc systems, the Hellenic arc involves a prominent slow wave speed ($\sim -4\%$) for the Aegean Sea down to nearly 100 km, a result of roll-back-induced back-arc extension⁸.

The Cenozoic Rift System, which is closely related to the central and western European volcanic fields⁶, extends from the Valencia Trough in Spain to the Massif Central in France, and then splits into two segments: one goes through the upper and lower Rhine Grabens in Germany and extends northwestward to the Netherlands, the other goes eastward to the Bohemian Massif in the Czech Republic, terminating in the Central Slovakian Volcanic Field (CSVF; Fig. 2a).

At 75 km depth, we also observe the Middle Hungarian Line, separating the CSVF and Tisza–Dacia (Fig. 2a). In the northern part of the Rhine Graben, we discover a slow anomaly ($\sim -2.5\%$) lying flat at a depth of approximately 300 km with a nearly vertical conduit ascending to the surface. We interpret these features as a slow-wave-speed reservoir connected through an upwelling plume, thereby forming the Eifel hotspot (Fig. 3e).

The North Anatolian Fault separates the fast-wave-speed Black Sea Basin and EEP to the north and the slow-wave-speed Anatolian plate to the south. The prominent slow anomaly of the Anatolian plate extends down to 220 km and overlays a large volume of fast anomalies ($\sim +3\%$; Fig. 2d), which we interpret as remnants of ancient oceanic lithosphere related to the collision between the Anatolian and African/Arabian plates. Beneath central Turkey, at a depth

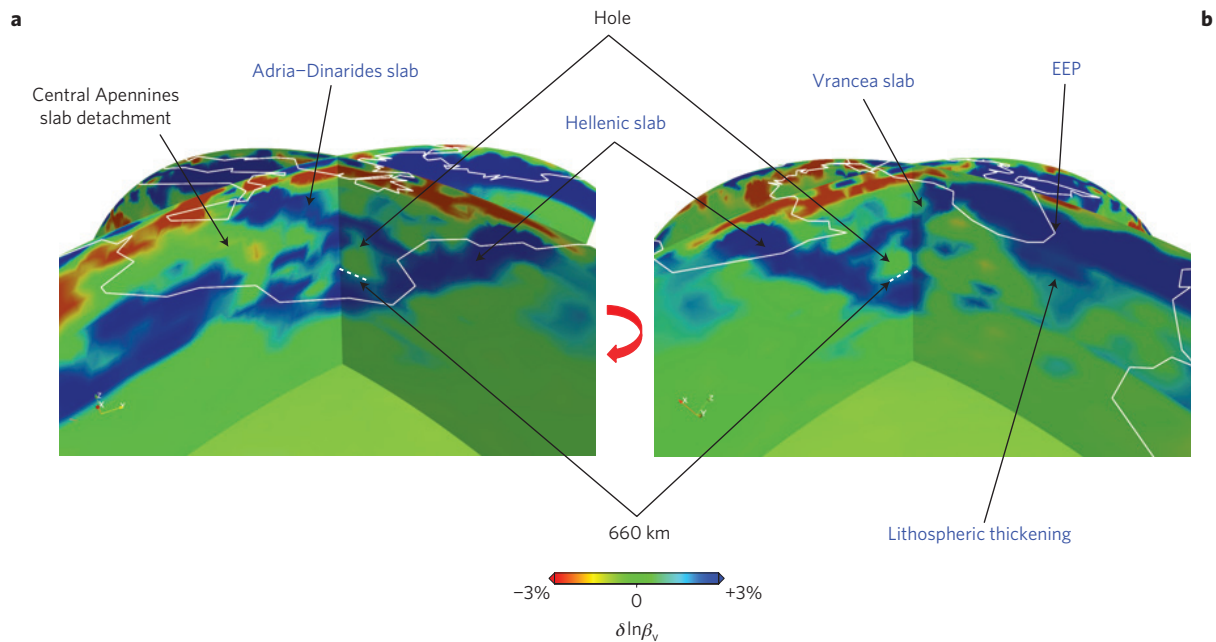


Figure 4 | 3D view of the interaction between the Adria-Dinarides, Vrancea and Hellenic slabs. The hole beneath Bulgaria is also shown. Relative perturbations in vertically polarized shear-wave speed $\delta \ln \beta_v$ are shown. White solid lines denote coast lines and white dashed lines denote the 660 km discontinuity. **b** is a right rotated view of **a**. EEP, East European Platform.

of 75 km, there is a structure surrounded by strong slow anomalies that coincides with the location of the Kirsehir Massif (Fig. 2a).

Owing to the demanding computational requirements for adjoint tomography, it is difficult to carry out traditional resolution tests, because these take the same amount of computational resources as the actual inversion. Here, we use the point-spread function³⁰ to assess image quality of the slab detachment beneath the central Apennines in intermediate model EU₁₈ and final model EU₃₀. The resolution tests confirm the quality of the images of this slab detachment (see Supplementary Figs S12 and S13), thereby lending support to our palaeotectonic interpretations.

Model EU₃₀ is described in terms of transversely isotropic shear-wave speeds and bulk-sound speed. The topography of primary interfaces (Moho and upper-mantle discontinuities) remains fixed, general anisotropy is not permitted and attenuation remains unchanged. These are parameters that are specified in the forward model but are not used in the inverse problem, and they constitute possible future extensions of this research. Addition of frequency-dependent amplitude measurements, complementing the travel-time measurements, should help to constrain these new parameters.

Received 16 November 2011; accepted 21 May 2012;
published online 24 June 2012

References

- Panza, G., Mueller, S. & Calcagnile, G. The gross features of the lithosphere–asthenosphere system in Europe from seismic surface and body waves. *Pure App. Geophys.* **118**, 1209–1213 (1980).
- Spakman, W. Subduction beneath Eurasia in connection with the Mesozoic Tethys. *Geologie en Mijnbouw* **65**, 145–153 (1986).
- Spakman, W. Delay time tomography of the upper mantle below Europe, the Mediterranean, and Asia Minor. *Geophys. J. Int.* **107**, 309–332 (1991).
- Spakman, W., van der Lee, S. & van der Hilst, R. Travel-time tomography of the European–Mediterranean mantle. *Phys. Earth Planet. Inter.* **79**, 3–74 (1993).
- Zielhuis, A. & Nolet, G. Shear-wave velocity variations in the upper mantle beneath central Europe. *Geophys. J. Int.* **117**, 695–715 (1994).
- Goes, S., Spakman, W. & Bijwaard, H. A lower mantle source for European volcanism. *Science* **286**, 1928–1931 (1999).
- Piromallo, C. & Morelli, A. P wave tomography of the mantle under the Alpine–Mediterranean area. *J. Geophys. Res.* **108**, B22065 (2003).
- Wortel, M. J. R. & Spakman, W. Subduction and slab detachment in the Mediterranean–Carpathian region. *Science* **290**, 1910–1917 (2000).
- Spakman, W. & Wortel, R. in *The TRANSMED Atlas, The Mediterranean Region from Crust to Mantle* (eds Cavazza, W., Roure, F. M., Spakman, W., Stampfli, G. & Ziegler, P.A.) 31–52 (Springer, 2004).
- Schmid, C., van der Lee, S., VanDecar, J., Engdahl, E. & Giardini, D. Three-dimensional S velocity of the mantle in the Africa-Eurasia plate boundary region from phase arrival times and regional waveforms. *J. Geophys. Res.* **113**, B03306 (2008).
- Koulakov, I., Kaban, M., Tesauro, M. & Cloetingh, S. P. and S- velocity anomaly in the upper mantle beneath Europe from tomographic inversion of ISC data. *Geophys. J. Int.* **179**, 345–366 (2009).
- Schivardi, R. & Morelli, A. EPmantle: A 3-D transversely isotropic model of the upper mantle under the European Plate. *Geophys. J. Int.* **185**, 469–484 (2011).
- Lippitsch, R., Kissling, E. & Ansgor, J. Upper mantle structure beneath the Alpine orogen from high-resolution teleseismic tomography. *J. Geophys. Res.* **108**, B82376 (2003).
- Mitterbauer, U. *et al.* Shape and origin of the east-Alpine slab constrained by the ALPASS teleseismic model. *Tectonophysics* **510**, 195–206 (2011).
- Komatitsch, D., Ritsema, J. & Tromp, J. The spectral-element method, Beowulf computing, and global seismology. *Science* **298**, 1737–1742 (2002).
- Tarantola, A. Linearized inversion of seismic reflection data. *Geophys. Prosp.* **32**, 998–1015 (1984).
- Akçelik, V. *et al.* High resolution forward and inverse earthquake modeling on terascale computers. *Proc. ACM/IEEE Supercomputing SC'2003 Conference* (2003). Published on CD-ROM and at www.sc-conference.org/sc2003.
- Tromp, J., Tape, C. & Liu, Q. Y. Seismic tomography, adjoint methods, time reversal and banana-doughnut kernels. *Geophys. J. Int.* **160**, 195–216 (2005).
- Chen, P., Zhao, L. & Jordan, T. H. Full 3D tomography for the crustal structure of the Los Angeles region. *Bull. Seismol. Soc. Am.* **97**, 1094–1120 (2007).
- Tape, C., Liu, Q. & Tromp, J. Finite-frequency tomography using adjoint methods—methodology and examples using membrane surface waves. *Geophys. J. Int.* **168**, 1105–1129 (2007).
- Tape, C., Liu, Q., Maggi, A. & Tromp, J. Adjoint tomography of the Southern California crust. *Science* **325**, 988–992 (2009).
- Tape, C., Liu, Q., Maggi, A. & Tromp, J. Seismic tomography of the southern California crust based on spectral-element and adjoint methods. *Geophys. J. Int.* **180**, 433–462 (2010).
- Molinari, I. & Morelli, A. EPcrust: A reference crustal model for the European Plate. *Geophys. J. Int.* **185**, 352–364 (2011).
- Kustowski, B., Ekström, G. & Dziewoński, A. M. Anisotropic shear-wave velocity structure of the Earth's mantle: A global model. *J. Geophys. Res.* **113**, B06306 (2008).
- Dziewoński, A. & Anderson, D. Preliminary Reference Earth model. *Phys. Earth Planet. Inter.* **25**, 297–356 (1981).

26. Hjörleifsdóttir, V. & Ekström, G. Effects of three-dimensional Earth structure on CMT earthquake parameters. *Phys. Earth Planet. Inter.* **179**, 178–190 (2010).
27. Maggi, A., Tape, C., Chen, M., Chao, D. & Tromp, J. An automated time window selection algorithm for seismic tomography. *Geophys. J. Int.* **178**, 257–281 (2009).
28. Amaru, M. *Geologica Ultraiectina*, Vol. 274, Ph.D. thesis, Utrecht Univ. (2007).
29. Dando, B. *et al.* Teleseismic tomography of the mantle in the Carpathian–Pannonian region of central Europe. *Geophys. J. Int.* **186**, 11–31 (2011).
30. Fichtner, A. & Trampert, J. Hessian kernels of seismic data functionals based upon adjoint techniques. *Geophys. J. Int.* **185**, 775–798 (2011).

Acknowledgements

We thank G. Houseman for comments on the structural interpretation and general suggestions that improved the manuscript. We thank J. Trampert and A. Fichtner for discussions regarding resolution analysis in full-waveform inversion and R. Wortel and W. Spakman for sharing their insights into Mediterranean tectonics. We acknowledge the Incorporated Research Institutions for Seismology (IRIS; <http://www.iris.edu>), Observatories and Research Facilities for European Seismology (<http://www.orfeus-eu.org>) and the Kandilli Observatory (<http://www.koeri.boun.edu.tr>) for providing the data used in this study. Numerical simulations were carried out on a Dell cluster built and maintained by the Princeton Institute for Computational Science

and Engineering. Data and synthetic processing was accomplished based on the Seismic Analysis Code (Goldstein, 2003). All maps and cross-sections were made with the Generic Mapping Tool (Wessel, 1991). The open-source spectral element software package SPECFEM3D_GLOBE and the seismic-measurement software package FLEXWIN used for this article are freely available for download through the Computational Infrastructure for Geodynamics (<http://www.geodynamics.org>). This research was supported by the US National Science Foundation under grant EAR-0711177.

Author contributions

H.J.Z. collected and analysed seismic data, carried out the inversion, interpreted the model and co-wrote the manuscript. E.B. collected seismic data from Program for Array Seismic Studies of the Continental Lithosphere (PASSCAL) and the Kandilli Observatory and interpreted the model. D.P. developed the calculation of transversely isotropic kernels and improved and optimized the spectral element and imaging software. J.T. planned the project, developed theory, interpreted the model, co-wrote the manuscript and provided overall guidance.

Additional information

The authors declare no competing financial interests. Supplementary information accompanies this paper on www.nature.com/naturegeoscience. Reprints and permissions information is available online at www.nature.com/reprints. Correspondence and requests for materials should be addressed to H.J.Z.